

Research paper

Phase-field based modeling and simulation for selective laser melting techniques in additive manufacturing

Sijing Lai^a, Qing Xia^a, Junseok Kim^b, Yibao Li^{a,*}^a School of Mathematics and Statistics, Xi'an Jiaotong University, Xi'an 710049, China^b Department of Mathematics, Korea University, Seoul 02841, Republic of Korea

ARTICLE INFO

Keywords:

Selective laser melting
Phase field method
Unconditional energy stability
Second order accuracy
Melt pool

ABSTRACT

In this study, we develop a phase-field model to describe the solid–liquid phase changes, heat conduction phenomena, during the selective laser melting process. This model is based on the variational principle of minimizing the free energy functional. The proposed model integrates the phase-field equation and the energy equation, which are used to capture the dynamical behavior of the interfacial evolution. We use the semi-implicit Crank–Nicolson scheme and central difference to ensure second-order accuracy in time and space. The numerical scheme is unconditional energy stable. This paper rigorously proves the energy stability of the phase-field model of the Selective Laser Melting process, which confirms the numerical stability and the physical rationality of the solution. Various numerical experiments are performed to verify the robustness of our proposal model. This model can effectively simulate the energy transfer and shape structure changes of the products during the selective laser melting manufacturing process, which provides a reliable guarantee for predicting and optimizing the quality and performance of the selective laser melting process additive manufacturing process.

1. Introduction

Selective Laser Melting (SLM) is an additive manufacturing technology that uses a laser beam to melt metal powder layer by layer, creating complex three-dimensional structures [1]. SLM process offers high flexibility and freedom, allowing precise control over material properties and geometric shapes, and can manufacture complex geometric shapes and functional parts that are difficult to achieve with traditional manufacturing methods [2]. Therefore, it has wide applications in aerospace, medical and automotive [3]. However, the SLM process involves multiple physical phenomena, posing significant challenges to the simulation and computation of the SLM process [4]. For example, the interaction of a laser beam with a metallic powder leads to a high temperature gradient and rapid cooling, affecting the microstructure and mechanical properties of the product. In addition, laser power and scanning speed affect the size and shape of the melt pool, while the effective diameter of the laser beam affects the cooling rate and stability of the melt pool [5,6]. Furthermore, the SLM process may introduce defects such as pores, cracks, and oxides, and residual stresses, affecting the quality and reliability of the parts [7,8]. To address these issues, an in-depth understanding and optimization of the SLM process is necessary to reveal its physical mechanisms and influence factors [9,10]. Since SLM processes involve complex coupled processes of multiple physical fields, multiple scales, and phase transitions, it is difficult to obtain comprehensive and accurate information. Furthermore, the current engineering experimental approaches are labor-intensive and time-consuming. Hence, it is imperative to formulate a mathematical model for this process and devise an efficient solution [11,12].

* Corresponding author.

E-mail address: yibaoli@xjtu.edu.cn (Y. Li).URL: <http://gr.xjtu.edu.cn/web/yibaoli> (Y. Li).<https://doi.org/10.1016/j.cnsns.2024.108239>

Received 8 April 2024; Received in revised form 12 June 2024; Accepted 17 July 2024

Available online 20 July 2024

1007-5704/© 2024 Elsevier B.V. All rights are reserved, including those for text and data mining, AI training, and similar technologies.

Numerous researchers have performed numerical simulations of the SLM process [13–15]. Ma et al. [16] utilized an improved high-order Smoothed Particle Hydrodynamics (SPH) method coupled with a cellular automaton to simulate the evolution of the solidification microstructure in the SLM process of 316L stainless steel. They investigated treatment impacts on the melt pool, employing a fluid dynamics method to simulate dynamic interactions within the melt pool. Nevertheless, the SPH method necessitates a substantial quantity of particles for depicting the fluid domain, inevitably leading to extensive computations. Chen et al. [17] used the level set method to establish a three-dimensional finite element model. This model was used to simulate the melting process of the powder, the formation of droplets, and the fluid dynamics within the melt pool. They studied the impact of Marangoni effect on ceramic trajectory in SLM, adeptly handling interface dynamics and topological changes, though demanding substantial computational resources. Liu et al. [18] used the thermal lattice Boltzmann and phase field methods to construct a multi-physics model, which simulates the evolution of the microstructure of alloy solidification during the SLM process. They analyzed the effect of latent heat, melt flow, and cooling rate on the solidification process. The thermal lattice Boltzmann method can simulate fluid flow and heat transfer. However, it requires high-resolution grids to capture complex interface morphologies. Additionally, it has difficulties in handling multi-component flow and multi-scale problems. Massimo et al. [19] used the Immersed Boundary method for thermo-mechanical analysis of the SLM process, simulating and evaluating the impact of residual stress on the mechanical performance and geometric accuracy of parts. However, it requires complex numerical algorithms to implement the enforcement of boundary conditions and suffers from shortcomings in dealing with large deformations and topological changes.

In order to simulate the multi-physics fields and thermodynamic processes in the SLM process, some researchers have employed the phase field method to model phase transitions, microstructure evolution [20–22], and heat conduction processes. The phase field method can consistently describe multi-scale, multi-physics phenomena and their coupled effects [23,24]. It characterizes transitions between different phases through a continuous phase change variable, avoiding the difficulty of tracking complex interfaces [25]. Moreover, it can consider the evolution of microstructures under non-equilibrium states [26–28], predicting the internal temperature distribution of materials and phase changes induced by temperature gradients. For instance, Sessim et al. [29] employed the phase-field approach to simulate the oxidation and thermal conduction processes in carbon fibers, examining the effects of fiber diameter, temperature, and airflow on oxidation. Zhang et al. [30] utilized the phase-field method to model the coupling process of pore migration driven by temperature gradients and thermal conduction. The results indicated that pores migrate towards regions of higher temperature, and a corresponding quantitative prediction equation was obtained. August et al. [31] applied the phase-field method to simulate the thermal conduction process in open-cell foams, integrating the diffuse interface representation with the heat transfer equation, yielding the effective thermal conductivity coefficients for different pore structures. Furthermore, various studies have employed the phase field method to simulate a range of processes in additive manufacturing. Sahoo et al. [32] employed a phase field model to simulate the microstructural evolution of Ti-6Al-4V titanium alloy in the electron beam additive manufacturing process, analyzing the effects of temperature gradients and laser beam scanning speed on microstructures. Liu et al. [33] utilized a 2D cellular automaton-phase field model to simulate the directed energy deposition process of Ti6Al4V, predicting microstructure and solute evolution. Yang et al. [34] devised a precise non-isothermal phase field model, capturing heat transfer, melt flow, and microstructure evolution during powder layer fusion. Yang et al. [35] employed a three-dimensional non-isothermal phase field simulation method to study the microstructural evolution in the selective laser sintering process, obtaining detailed results of key features such as porosity, surface morphology, temperature distribution, and densification. Xia et al. [36] proposed a multi-scale phase field model coupled with multi-physics fields to solve problems such as temperature fields, crystallization phenomena, and trajectory shapes in the fused deposition modeling process. The flexibility and applicability of the phase field method have made it widely used in materials science and engineering [37], becoming an effective tool for simulating phase transitions and microstructure evolution in various additive manufacturing processes.

To ensure the accuracy and reliability of the phase-field model in optimizing process parameters, it is necessary to conduct mathematical analysis and energy stability verification of the SLM manufacturing process. Energy-stable methods, verified through rigorous mathematical analysis, ensure the correctness of conservation and dissipation laws in numerical simulations. This is crucial for thermodynamic analysis and the accuracy of phase-field models in SLM processes. The rapid thermal and phase changes in SLM require precise calculations for realistic simulations. Energy-stable methods achieve stability and consistency by constructing numerical schemes that accurately reflect the energy changes in physical systems [38,39]. They also enhanced computational efficiency by allowing larger time steps, reducing computation time [40,41]. Furthermore, these methods ensure numerical simulations align with physical processes by accurately modeling energy changes during heat conduction and phase transitions [42,43]. The development of energy-stable methods originated from the exploration of energy conservation in simple physical systems. Early numerical methods, such as explicit and implicit time discretization methods, were effective in simple systems, but numerical instabilities in complex systems limited their applications. For instance, while explicit methods are computationally simple, they require extremely small time steps to maintain stability, which limits their range of applications. With technological advances, high-order time discretization methods such as Crank–Nicolson (CN) and Runge–Kutta methods have emerged. Their high accuracy and stability in time integration significantly enhance the modeling capabilities for complex systems. In particular, the CN method, with its energy stability and high-order accuracy, has found a wide range of applications in simulations of thermal conduction and phase transitions. In further studies, variational and numerical methods based on dissipative structures have come into focus [44,45]. Variational approaches introduce new numerical integration and time discretization techniques to construct numerical schemes that accurately reflect energy variations. For example, methods based on variational inequalities optimize the energy function to ensure long-term numerical stability [46,47]. Numerical methods based on dissipative structures, such as the Scalar Auxiliary Variable (SAV) method, ensure the accuracy and stability of numerical simulation through auxiliary variables, effectively solving the energy

dissipation problem in complex fields [48]. Recently, significant progress has been made in energy stabilization methods for phase-field models. Han et al. [49] developed a second-order fully discrete scheme to model the phase field of a two-phase incompressible fluid, verifying its stability and accuracy in complex domains. Yang et al. [50] proposed an efficient energy stabilization scheme based on the SAV method for simulating a two-phase incompressible model of a conservative Allen-Cahn fluid, showing superior performance in large-scale calculations.

In this paper, we will develop a phase field model capable of accurately simulating the solid-liquid phase transition and heat conduction phenomena during selective laser melting. The model is based on the variational principle of minimizing the free energy functional, and the agreement with the thermodynamic laws is maintained. The model is discretized using the semi-implicit CN scheme, which ensures second-order accuracy in time and space. This paper rigorously proves the energy stability of the phase-field model of the SLM process, which confirms the numerical stability and the physical rationality of the solution. It guarantees that the proposed numerical scheme can maintain the energy dissipation properties of the governing equations regardless of the chosen time step. We both numerically showcase how the proposed model effectively captures interface morphology and heat radiation. Additionally, we present evidence supporting the numerical stability and efficiency of our model. This contributes to accurate predictions and improvements in product quality and performance in the additive manufacturing process of the SLM technology.

The paper is organized as follows: Section 2 introduces the phase-field model of the SLM process and derives its governing equations. Section 3 provides the numerical scheme for solving the model and demonstrates its accuracy and stability. Section 4 conducts various numerical experiments. Finally, Section 5 provides a conclusive review of the paper.

2. Methodology

In order to establish a thermodynamics consistently model, we use the entropy method to derive energy and phase field equations that preserve thermodynamic consistency. To accurately capture the dynamic phase transition between solid and liquid states, we introduce the phase field variable $\phi \in [0, 1]$. The phase field variable takes on $\phi = 1$ for the liquid phase and $\phi = 0$ for the solid phase, respectively. By considering the gradient effect, the entropy functional of the system is composed of the entropy density in the homogeneous bulk phase and the spatial variation of the phase field function over the material volume Ω . This can be stated as follows:

$$S = \int_{\Omega} \left(s(e, \phi) - \frac{1}{2} \xi_{\phi}^2 |\nabla \phi|^2 \right) d\mathbf{x}, \quad (1)$$

where the gradient effect $|\nabla \phi|^2$ is related to the interfacial energy. Here $s(e, \phi)$ is the local entropy density, which is a function of the internal energy density e and the corresponding phase variable ϕ . Let us start from the variational derivative

$$\frac{\partial e}{\partial t} = -\nabla \cdot \left(M_e \nabla \frac{\delta S}{\delta e} \right), \quad (2)$$

$$\frac{\partial \phi}{\partial t} = M_{\phi} \frac{\delta S}{\delta \phi}. \quad (3)$$

The apparent mobility coefficient M_e is defined as $T^2 k(T)$, where $k(T)$ is the temperature-dependent thermal conductivity determined by the material properties, phase field, and temperature field. Meanwhile, M_{ϕ} represents the constant mobility at the solid-liquid interface during powder melting, ξ_{ϕ} is the diffusion coefficient depends on the apparent thickness and mobility. In the above equations, the variational derivatives are given by

$$\frac{\delta S}{\delta e} = \frac{\partial s(e, \phi)}{\partial e} = \frac{1}{T}, \quad (4)$$

$$\frac{\delta S}{\delta \phi} = \frac{\partial s(e, \phi)}{\partial \phi} + \xi_{\phi}^2 \nabla^2 \phi. \quad (5)$$

To evaluate the free energy density $f(T, \phi)$, the internal energy density is postulated

$$e(T, \phi) = e_s(T) + p(\phi)L(T) = e_l(T) + p(\phi)(e_l(T) - e_s(T)), \quad (6)$$

where $e_s(T)$ and $e_l(T)$ are the classical internal energy densities of the solid and liquid phases, respectively. $L(T) = e_l(T) - e_s(T)$ is the latent heat of fusion. Additionally, the polynomial interpolation function $p(\phi)$ is defined as $p(\phi) = \phi^3(10 - 15\phi + 6\phi^2)$, which follows the thermodynamically consistent phase-field approach. This interpolation function satisfies the conditions $p(0) = 0$, $p(1) = 1$, and $dp/d\phi = d^2p/d\phi^2 = 0$ at both $\phi = 0$ and $\phi = 1$. Assuming constant and equal values for the specific heat C in both phases, the energy densities $e_s(T)$ and $e_l(T)$ are given by

$$e_l(T) = e_l(T_m) + C(T - T_m), \quad (7)$$

$$e_s(T) = e_s(T_m) + C(T - T_m). \quad (8)$$

Here, T_m represents the equilibrium melting temperature of the pure metallic powders. The difference $L_a = L(T_m)$ gives the latent heat per unit volume of fusion. Referring to [51], we can write $f(T, \phi)$ as

$$f(T, \phi) = \left(e_s(T_m) - CT_m + p(\phi)L_a \right) \left(1 - \frac{T_m}{T} \right) - CT \ln \left(\frac{T}{T_m} \right) + TG(\phi). \quad (9)$$

The function $G(\phi)$ is defined as $G(\phi) = \phi^2(1 - \phi)^2/4$, which takes the form of a symmetric double well potential with minima at both $\phi = 0$ and $\phi = 1$. Using the thermodynamic equation

$$\left(\frac{\partial s}{\partial \phi}\right)_e = -\frac{1}{T} \left(\frac{\partial f}{\partial \phi}\right)_T, \quad (10)$$

and Eqs. (3),(7),(9), the dynamic evolution of the phase field can be yielded as

$$\frac{d\phi}{dt} = M_\phi \left(\xi_\phi^2 \Delta \phi + p'(\phi) L_a \frac{T - T_m}{TT_m} - G'(\phi) \right). \quad (11)$$

The evolution of the thermal field is easily derived from Eqs. (2),(4) and (6):

$$\frac{\partial T}{\partial t} + M_\phi L_a \frac{p'(\phi)}{TT_m} \frac{\partial \phi}{\partial t} = k \nabla^2 T. \quad (12)$$

Thus, we can get the governing equation as follows:

$$\frac{\partial \phi}{\partial t} = M_\phi \left(\xi_\phi^2 \Delta \phi + p'(\phi) L_a \frac{T - T_m}{TT_m} - G'(\phi) \right), \quad (13a)$$

$$\frac{\partial T}{\partial t} + M_\phi \frac{L_a}{TT_m} p'(\phi) \frac{\partial \phi}{\partial t} = k \Delta T. \quad (13b)$$

In model (13a), concerning the equation for ϕ , we have introduced a term $M_\phi p'(\phi) L_a (T - T_m) / (TT_m)$ related to temperature. This term accounts for the Gibbs-Thomson effect and kinetic effects during solidification, considering the thermal driving force due to high temperature and latent heat during the solid–liquid phase transition of metal powder. The first and third terms on the right side of Eq. (13a) represent the balance of diffusive and double-well phase separation effects, respectively, leading to the formation and evolution of smooth and narrow interface profiles. In the temperature Eq. (13b), the temperature change is determined by both heat conduction and the latent heat effect of solid–liquid phase transition. We consider the bidirectional coupling phenomenon of phase transition and thermal diffusion effects in the SLM process. This allows our model to accurately predict the temperature distribution during the SLM process and capture the evolution of the phase field caused by temperature changes. In addition, we ensure the convergence of the algorithm through the proof of continuous energy and discrete energy reduction, and verify the solvability of the system through numerical simulation. This implies that our model is highly coupled with the real physical process and complies with the laws of thermodynamics. Then we can get the following energy dissipation law. To elaborate, we utilize (\cdot, \cdot) to represent the L_2 inner product and $\|\cdot\|^2$ to denote the L_2 norm.

Theorem 1. *The solutions of the hybrid system composed by Eqs. (13) satisfies the energy dissipation law, i.e.*

$$\frac{dE}{dt} = -\left\| \frac{\partial \phi}{\partial t} \right\|^2 - k \|\nabla(T - T_m)\|^2 \leq 0,$$

where the energy is defined as

$$E = \int_{\Omega} M_\phi G(\phi) d\mathbf{x} + \frac{1}{2} \|T - T_m\|^2 + \frac{M_\phi}{2} \xi_\phi^2 \|\nabla \phi\|^2. \quad (14)$$

Proof. Let us take the derivative of the total energy with respect to time as

$$\frac{dE}{dt} = \left(T - T_m, \frac{\partial T}{\partial t} \right) + M_\phi \left(G'(\phi), \frac{\partial \phi}{\partial t} \right) + M_\phi \xi_\phi^2 \left(\nabla \phi, \frac{\partial \nabla \phi}{\partial t} \right). \quad (15)$$

Then, we take the L_2 inner product of Eq. (13a) with $\partial \phi / \partial t$ as follows:

$$\left(\frac{\partial \phi}{\partial t}, \frac{\partial \phi}{\partial t} \right) = -M_\phi \xi_\phi^2 \left(\Delta \phi, \frac{\partial \phi}{\partial t} \right) + M_\phi L_a \left(p'(\phi) \frac{T - T_m}{TT_m}, \frac{\partial \phi}{\partial t} \right) - M_\phi \left(G'(\phi), \frac{\partial \phi}{\partial t} \right). \quad (16)$$

By taking L_2 inner product of Eq. (13b) with $(T - T_m)$, we can get

$$\left(\frac{\partial T}{\partial t}, T - T_m \right) + M_\phi L_a \left(p'(\phi) \frac{T - T_m}{TT_m}, \frac{\partial \phi}{\partial t} \right) = (k \Delta T, T - T_m). \quad (17)$$

Thus we can obtain the dissipate energy functional as

$$\begin{aligned} \frac{dE}{dt} &= \left(T - T_m, \frac{\partial T}{\partial t} \right) + M_\phi \left(G(\phi), \frac{\partial \phi}{\partial t} \right) + M_\phi \xi_\phi^2 \left(\nabla \phi, \frac{\partial \nabla \phi}{\partial t} \right) \\ &= -\left\| \frac{\partial \phi}{\partial t} \right\|^2 - k \|\nabla(T - T_m)\|^2 \leq 0, \end{aligned}$$

which completes the proof. \square

To effectively handle the nonlinear terms in the energy functional and achieve a fully decoupled linear system. Let us define the auxiliary variable $r(t)$ as follows:

$$r(t) = \sqrt{\int_{\Omega} G(\phi) d\mathbf{x} + B}, \quad (18)$$

where B is a large enough positive constant such that $r(t)$ is positive, and B should satisfy $B > -\int_{\Omega} G(\phi) d\mathbf{x}$. By taking the time derivative of the new variable $r(t)$, we rewrite the system Eqs. (13) as the following equivalent system:

$$\frac{d\phi}{dt} = M_{\phi} \left(\xi_{\phi}^2 \Delta \phi + p'(\phi) L_a \frac{T - T_m}{TT_m} - r Z_{\phi} \right), \quad (19a)$$

$$\frac{\partial T}{\partial t} + M_{\phi} \frac{L_a}{TT_m} p'(\phi) \frac{\partial \phi}{\partial t} = k \Delta T, \quad (19b)$$

$$\frac{dr}{dt} = \frac{1}{2} \int_{\Omega} Z_{\phi} \frac{d\phi}{dt} d\mathbf{x} = \frac{1}{2} \left(Z_{\phi}, \frac{\partial \phi}{\partial t} \right), \quad (19c)$$

where $Z_{\phi} = G'(\phi) / \sqrt{\int_{\Omega} G(\phi) d\mathbf{x} + B}$, $G'(\phi) = r Z_{\phi}$. Thus, the total free energy (14) can be rewritten as:

$$E = \int_{\Omega} \left(M_{\phi} r^2(t) - M_{\phi} B \right) d\mathbf{x} + \frac{1}{2} \|T - T_m\|^2 + \frac{M_{\phi}}{2} \xi_{\phi}^2 \|\nabla \phi\|^2. \quad (20)$$

Then we can obtain the energy dissipation law of the new system Eq. (19) as follows:

$$\begin{aligned} \frac{dE}{dt} &= \left(T - T_m, \frac{\partial T}{\partial t} \right) + M_{\phi} \xi_{\phi}^2 \left(\nabla \phi, \frac{\partial \nabla \phi}{\partial t} \right) + M_{\phi} \left(r Z_{\phi}, \frac{\partial \phi}{\partial t} \right) \\ &= - \left\| \frac{\partial \phi}{\partial t} \right\|^2 - k \|\nabla(T - T_m)\|^2 \leq 0. \end{aligned} \quad (21)$$

Remark 1. In our model (13), we consider the bidirectional coupling phenomenon of phase change and temperature during the SLM process, introducing a new term $M_{\phi} p'(\phi) L_a (T - T_m) / (TT_m)$. This turns our model into a highly coupled nonlinear equation. To address this challenge, we choose the SAV approach and further construct a second-order accurate SAV-CN scheme. Currently, there are many other energy-stable methods to deal with phase-field models, such as the Lagrange multiplier method [52], Invariant Energy Quadratization [53], etc. The SAV method simplifies the numerical treatment of the strong nonlinearities present in the coupled phase transition and temperature field by introducing auxiliary variables that transform the nonlinear terms into linear ones. We combine the SAV method with the CN discretization to obtain a robust and efficient numerical scheme that achieves second-order accuracy in both time and space. This is crucial to accurately model the dynamics of phase boundaries and thermal gradients during the SLM process. With the SAV approach, we ensure the physical plausibility of the model and show that it satisfies the second law of thermodynamics and the conservation properties of energy decay, thus maintaining the thermodynamic consistency of the model.

3. Discrete schemes and energy dissipation

Let us introduce the discrete operators and formulation with the second-order central difference method. We illustrate the discrete system by considering the 3D domain $\Omega_p^d = [0, L_x] \times [0, L_y] \times [0, L_z]$. We discretize the computational domain with a uniform mesh grid, whose mesh size is computed as $h = L_x/N_x = L_y/N_y = L_z/N_z$ with the positive even integers N_x , N_y and N_z on the x -, y - and z - directions, respectively. Let us denote i , j and k as the directional index, thus we can define ϕ_{ij}^n as the approximation to $\phi(x_i, y_j, z_k, n\Delta t)$, where $x_i = (i - 0.5)h$, $y_j = (j - 0.5)h$, $z_k = (k - 0.5)h$, $\Delta t = T/N$, T is the final time, and N is the total time step. To elaborate, we utilize $(\cdot, \cdot)_d$ to represent the discrete L_2 inner product and $\|\cdot\|_d^2$ to denote the discrete L_2 norm. In this section, we present the second-order time discrete schemes. For convenience, we have conducted the following notation throughout this paper

$$\phi^{n+\frac{1}{2}} = (\phi^{n+1} + \phi^n)/2, \quad \hat{\phi}^{n+\frac{1}{2}} = (3\phi^n - \phi^{n-1})/2, \quad (22a)$$

$$T^{n+\frac{1}{2}} = (T^{n+1} + T^n)/2, \quad \hat{T}^{n+\frac{1}{2}} = (3T^n - T^{n-1})/2, \quad (22b)$$

$$\hat{r}^{n+\frac{1}{2}} = (3r^n - r^{n-1})/2, \quad \hat{Z}_{\phi}^{n+\frac{1}{2}} = (3Z_{\phi}^n - Z_{\phi}^{n-1})/2. \quad (22c)$$

We develop the following numerical scheme based on the Crank–Nicolson temporal discretization:

$$\frac{\phi^{n+1} - \phi^n}{\Delta t} = M_{\phi} \left(\xi_{\phi}^2 \Delta_d \phi^{n+\frac{1}{2}} + L_a p'(\hat{\phi}^{n+\frac{1}{2}}) \frac{T^{n+\frac{1}{2}} - T_m}{\hat{T}^{n+\frac{1}{2}} T_m} - \hat{r}^{n+\frac{1}{2}} \hat{Z}_{\phi}^{n+\frac{1}{2}} \right), \quad (23a)$$

$$\frac{T^{n+1} - T^n}{\Delta t} + \frac{M_{\phi} L_a}{\hat{T}^{n+\frac{1}{2}} T_m} p'(\hat{\phi}^{n+\frac{1}{2}}) \frac{\phi^{n+1} - \phi^n}{\Delta t} = k \Delta_d T^{n+\frac{1}{2}}, \quad (23b)$$

$$\frac{r^{n+1} - r^n}{\Delta t} = \frac{1}{2} \left(\hat{Z}_{\phi}^{n+\frac{1}{2}}, \frac{\phi^{n+1} - \phi^n}{\Delta t} \right)_d. \quad (23c)$$

According to the discrete system (23), we can give the system of linear equations as follows:

$$\begin{pmatrix} 2I_d/\Delta t - M_{\phi} \xi_{\phi}^2 \Delta_d & -M_{\phi} L_a p'(\hat{\phi}^{n+\frac{1}{2}})/(\hat{T}^{n+\frac{1}{2}} T_m) \\ M_{\phi} L_a p'(\hat{\phi}^{n+\frac{1}{2}})/(\hat{T}^{n+\frac{1}{2}} T_m) & I_d - k \Delta_d \Delta_d/2 \end{pmatrix} \begin{pmatrix} \phi^{n+1} \\ T^{n+1} \end{pmatrix} = \begin{pmatrix} f_1 \\ f_2 \end{pmatrix}, \quad (24)$$

where Δ_d is the Laplacian operator under the finite difference framework. I_d is the standard Identity discrete operator in finite difference framework. The components in the source term are as follows:

$$f_1 = \left(\frac{2}{\Delta t} I_d + M_\phi \xi_\phi^2 \Delta_d \right) \phi^n + \frac{M_\phi L_a p'(\hat{\phi}^{n+\frac{1}{2}})}{\hat{T}^{n+\frac{1}{2}} T_m} T^n - M_\phi \hat{Z}_\phi^{n+\frac{1}{2}} \hat{r}^{n+\frac{1}{2}} - \frac{2M_\phi L_a p'(\hat{\phi}^{n+\frac{1}{2}})}{\hat{T}^{n+\frac{1}{2}}}, \quad (25)$$

$$f_2 = \frac{M_\phi L_a p'(\hat{\phi}^{n+\frac{1}{2}})}{\hat{T}^{n+\frac{1}{2}} T_m} \phi^n + \left(I_d + \frac{k\Delta t}{2} \Delta_d \right) T^n. \quad (26)$$

We employ the SAV method to deal with the nonlinear terms, resulting in a fully decoupled linear system. The feature of complete decoupling reduces the computational complexity, enabling the possibility of parallel computation and hence enhancing computational efficiency. The linearized system minimizes the error in the solution process, rendering the numerical solution more accurate and stable. We employ the Bi-Conjugate Gradient Stabilized Method (BiCGSTAB) to solve this linear system at the semi-implicit time level. The BiCGSTAB algorithm provides faster convergence rates for fully decoupled linear systems, implying that higher accuracy can be achieved within the same computational timeframe. Moreover, due to its stability, the method is capable of effectively mitigating numerical oscillations induced by time-stepping variations, even when operating at the semi-implicit temporal level. Herein, we can drive the unconditional energy stability of the numerical scheme Eq. (23) as follows.

Theorem 2. *The solutions of the discrete system satisfies the modified energy dissipation law, i.e.*

$$\frac{E^{n+1} - E^n}{\Delta t} = -\frac{k}{4} \left\| \nabla_d (T^{n+1} + T^n - 2T_m) \right\|_d^2 - \left\| \frac{\phi^{n+1} - \phi^n}{\Delta t} \right\|_d^2 \leq 0, \quad (27)$$

where the modified energy is defined as

$$E^n = \frac{1}{2} \|T^n - T_m\|_d^2 + \frac{M_\phi}{2} \xi_\phi^2 \|\nabla_d \phi^n\|_d^2 + 2M_\phi r^n \hat{r}^{n+\frac{1}{2}}. \quad (28)$$

Proof. Let us take the L_2 inner product of Eq. (23a) with $(\phi^{n+1} - \phi^n)/\Delta t$ as follows:

$$\begin{aligned} \left(\frac{\phi^{n+1} - \phi^n}{\Delta t}, \frac{\phi^{n+1} - \phi^n}{\Delta t} \right)_d &= M_\phi \xi_\phi^2 \left(\Delta_d \phi^{n+\frac{1}{2}}, \frac{\phi^{n+1} - \phi^n}{\Delta t} \right)_d - M_\phi \left(\hat{r}^{n+\frac{1}{2}} \hat{Z}_\phi^{n+\frac{1}{2}}, \frac{\phi^{n+1} - \phi^n}{\Delta t} \right)_d \\ &\quad + M_\phi L_a \left(p'(\hat{\phi}^{n+\frac{1}{2}}) \frac{T^{n+\frac{1}{2}} - T_m}{\hat{T}^{n+\frac{1}{2}} T_m}, \frac{\phi^{n+1} - \phi^n}{\Delta t} \right)_d, \end{aligned} \quad (29)$$

which can be rearranged as

$$\begin{aligned} \frac{M_\phi \xi_\phi^2}{2\Delta t} \left(\|\nabla_d \phi^{n+1}\|_d^2 - \|\nabla_d \phi^n\|_d^2 \right) &= - \left\| \frac{\phi^{n+1} - \phi^n}{\Delta t} \right\|_d^2 - M_\phi \left(\hat{r}^{n+\frac{1}{2}} \hat{Z}_\phi^{n+\frac{1}{2}}, \frac{\phi^{n+1} - \phi^n}{\Delta t} \right)_d \\ &\quad + M_\phi L_a \left(p'(\hat{\phi}^{n+\frac{1}{2}}) \frac{T^{n+\frac{1}{2}} - T_m}{\hat{T}^{n+\frac{1}{2}} T_m}, \frac{\phi^{n+1} - \phi^n}{\Delta t} \right)_d. \end{aligned} \quad (30)$$

Then, we take the L_2 inner product of Eq. (23b) with $(T^{n+\frac{1}{2}} - T_m)$ as follows:

$$\begin{aligned} \left(\frac{T^{n+1} - T^n}{\Delta t}, T^{n+\frac{1}{2}} - T_m \right)_d &+ M_\phi L_a \left(p'(\hat{\phi}^{n+\frac{1}{2}}) \frac{T^{n+\frac{1}{2}} - T_m}{\hat{T}^{n+\frac{1}{2}} T_m}, \frac{\phi^{n+1} - \phi^n}{\Delta t} \right)_d \\ &= k \left(\Delta_d T^{n+\frac{1}{2}}, T^{n+\frac{1}{2}} - T_m \right)_d, \end{aligned} \quad (31)$$

where

$$\left(\frac{T^{n+1} - T^n}{\Delta t}, T^{n+\frac{1}{2}} - T_m \right)_d = \frac{1}{2\Delta t} \left(\|T^{n+1} - T_m\|_d^2 - \|T^n - T_m\|_d^2 \right). \quad (32)$$

The right-hand side of Eq. (31) can be rewritten as

$$k \left(\Delta_d T^{n+\frac{1}{2}}, T^{n+\frac{1}{2}} - T_m \right)_d = -\frac{k}{4} \left\| \nabla_d (T^{n+1} + T^n - 2T_m) \right\|_d^2. \quad (33)$$

By taking Eq. (32) to Eq. (33), we can obtain

$$\begin{aligned} &\frac{1}{2\Delta t} \left(\|T^{n+1} - T_m\|_d^2 - \|T^n - T_m\|_d^2 \right) \\ &= -M_\phi L_a \left(p'(\hat{\phi}^{n+\frac{1}{2}}) \frac{T^{n+\frac{1}{2}} - T_m}{\hat{T}^{n+\frac{1}{2}} T_m}, \frac{\phi^{n+1} - \phi^n}{\Delta t} \right)_d - \frac{k}{4} \left\| \nabla_d (T^{n+1} + T^n - 2T_m) \right\|_d^2. \end{aligned} \quad (34)$$

After that, let us take the L_2 inner product of Eq. (23c) with $\hat{r}^{n+\frac{1}{2}}$ as follows:

$$\left(\frac{r^{n+1} - r^n}{\Delta t}, \hat{r}^{n+\frac{1}{2}} \right)_d = \frac{1}{2} \left(\hat{r}^{n+\frac{1}{2}} \hat{Z}_\phi^{n+\frac{1}{2}}, \frac{\phi^{n+1} - \phi^n}{\Delta t} \right)_d, \quad (35)$$

which can be rearranged as

$$\frac{2M_\phi}{\Delta t} \hat{r}^{n+\frac{1}{2}} (r^{n+1} - r^n) = M_\phi \left(\hat{r}^{n+\frac{1}{2}} \hat{Z}_\phi^{n+\frac{1}{2}}, \frac{\phi^{n+1} - \phi^n}{\Delta t} \right)_d. \quad (36)$$

By combining Eq. (30), (34) and (36), we have the following modified energy dissipation law:

$$\begin{aligned} \frac{E^{n+1} - E^n}{\Delta t} &= \frac{1}{2\Delta t} (\|T^{n+1} - T_m\|_d^2 - \|T^n - T_m\|_d^2) + \frac{M_\phi \xi_\phi^2}{2\Delta t} (\|\nabla_d \phi^{n+1}\|_d^2 - \|\nabla_d \phi^n\|_d^2) \\ &\quad + \frac{2M_\phi}{\Delta t} \hat{r}^{n+\frac{1}{2}} (r^{n+1} - r^n) \\ &= -M_\phi L_a \left(p'(\hat{\phi}^{n+\frac{1}{2}}) \frac{T^{n+\frac{1}{2}} - T_m}{\hat{T}^{n+\frac{1}{2}} T_m}, \frac{\phi^{n+1} - \phi^n}{\Delta t} \right)_d - \frac{k}{4} \|\nabla_d (T^{n+1} + T^n - 2T_m)\|_d^2 \\ &\quad - M_\phi \left(\hat{r}^{n+\frac{1}{2}} \hat{Z}_\phi^{n+\frac{1}{2}}, \frac{\phi^{n+1} - \phi^n}{\Delta t} \right)_d + M_\phi L_a \left(p'(\hat{\phi}^{n+\frac{1}{2}}) \frac{T^{n+\frac{1}{2}} - T_m}{\hat{T}^{n+\frac{1}{2}} T_m}, \frac{\phi^{n+1} - \phi^n}{\Delta t} \right)_d \\ &\quad - \left\| \frac{\phi^{n+1} - \phi^n}{\Delta t} \right\|_d^2 + M_\phi \left(\hat{r}^{n+\frac{1}{2}} \hat{Z}_\phi^{n+\frac{1}{2}}, \frac{\phi^{n+1} - \phi^n}{\Delta t} \right)_d \\ &= -\frac{k}{4} \|\nabla_d (T^{n+1} + T^n - 2T_m)\|_d^2 - \left\| \frac{\phi^{n+1} - \phi^n}{\Delta t} \right\|_d^2 \leq 0. \end{aligned}$$

This completes the proof. \square

Theorem 3. With the computed variables: $\hat{\phi}^{n+\frac{1}{2}}, \hat{T}^{n+\frac{1}{2}}$, there exist unique solutions ϕ^{n+1}, T^{n+1} of Eq. (23).

Proof. According to Eq. (24), we can get the block coefficient matrix \mathcal{A} of the linear system (23) as follows:

$$\mathcal{A} = \begin{pmatrix} 2I_d/\Delta t - M_\phi \xi_\phi^2 \Delta_d & -M_\phi L_a p'(\hat{\phi}^{n+\frac{1}{2}})/(\hat{T}^{n+\frac{1}{2}} T_m) \\ M_\phi L_a p'(\hat{\phi}^{n+\frac{1}{2}})/(\hat{T}^{n+\frac{1}{2}} T_m) & I_d - k\Delta t \Delta_d/2 \end{pmatrix}. \quad (37)$$

Let us set $A_{11} = 2I_d/\Delta t - M_\phi \xi_\phi^2 \Delta_d$, $A_{22} = I_d - k\Delta t \Delta_d/2$, $A_{12} = -A_{21} = M_\phi L_a p'(\hat{\phi}^{n+\frac{1}{2}})/(\hat{T}^{n+\frac{1}{2}} T_m)$. Given that I_d is the identity operator and Δ_d is a semi-negative definite Laplacian operator, it follows that matrices A_{11} and A_{22} are positive definite. Inspired by [54], the Schur complement S for the block matrix \mathcal{A} is given by

$$S = A_{22} - A_{21} A_{11}^{-1} A_{12}, \quad (38)$$

where

$$A_{21} A_{11}^{-1} A_{12} = - \left(\frac{M_\phi L_a p'(\hat{\phi}^{n+\frac{1}{2}})}{\hat{T}^{n+\frac{1}{2}} T_m} \right) A_{11}^{-1} \left(\frac{M_\phi L_a p'(\hat{\phi}^{n+\frac{1}{2}})}{\hat{T}^{n+\frac{1}{2}} T_m} \right). \quad (39)$$

Let us denote $B = M_\phi L_a p'(\hat{\phi}^{n+\frac{1}{2}})/(\hat{T}^{n+\frac{1}{2}} T_m)$, then we have $S = A_{22} + B A_{11}^{-1} B$, which is also positive definite. According to the Schur complement property of the block matrix [55], it can be deduced that the block matrix \mathcal{A} is positive definite. Consequently, the coefficient matrix \mathcal{A} of the linear system (23) is invertible. Therefore, the system (23) has a unique solution. \square

4. Numerical experiments

In this section, we perform several numerical simulations in two and three-dimensions, such as energy dissipation experiments, stability experiments, precision experiments, 3D layer-by-layer printing evolution experiments, and comparison experiments with different layer thickness. Unless otherwise specified, we set the 3D domain $\Omega_p^d = [0, 1] \times [0, 1] \times [0, 1]$. The following parameter settings were chosen: $T_m = 50$, $M_\phi = 1$, $L_a = 1$, $\xi_\phi = 4h/(2\sqrt{2}\text{atanh}(0.9))$, $k = 2$, $B = 10^3$, $\eta = 1$, $\rho = 1$, and $\Delta t = 0.1h$.

4.1. Numerical stability

In this section, we numerically verify that the proposed system satisfies the energy dissipation law and validate the energy stability of the system at four different time steps. We normalize both the corrected energy and the original energy by the initial energy, with the initial conditions set as follows:

$$\phi(x, y, 0) = -0.5 \tanh \left(\frac{\sqrt{(x-0.5)^2 + (y-0.5)^2} - 0.16(0.9 + 0.36(\cos(6\theta) + \sin(6\theta)))}{\sqrt{2}\xi_\phi} \right) + 0.5,$$

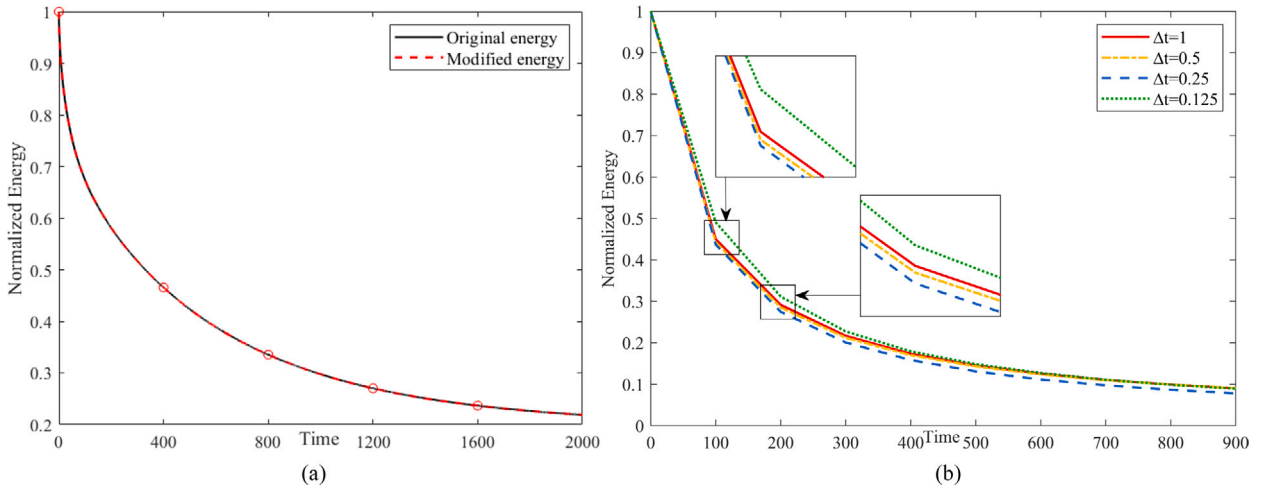


Fig. 1. (a) is the evolution of the initial energy over time normalized by the original energy and the discrete corrected energy. (b) is a plot of the normalized energy functional over time at four different time steps $\Delta t = 1, 0.5, 0.25$, and 0.125 . The two subgraphs are local curve enlargements at the two turning points.

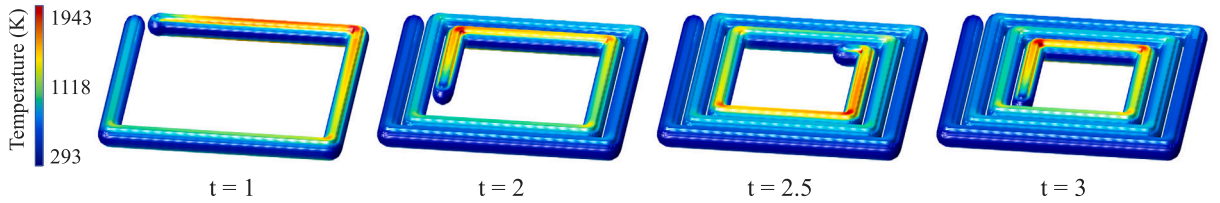


Fig. 2. Simulation of the manufacturing process of a single-layer spiral model. From left to right, the simulated effects of the single-layer spiral at specific times $t = 1, 2, 2.5$, and 3 , respectively.

$$T(x, y, 0) = 100\phi(x, y, 0) + 1.$$

As illustrated in Fig. 1(a), the corrected energy curve exhibits a decaying trend over time, consistent with the original energy curve. Furthermore, we choose $\phi(x, y, 0) = \text{rand}(x, y, z)$ to corroborate the energy dissipation and stability of the system at four distinct time steps. To demonstrate the stability of the proposed scheme, we conduct numerical experiments at different time steps $\Delta t = 1, 0.5, 0.25$, and 0.125 . As shown in Fig. 1(b), we compare the evolution of the total energy at different time steps $\Delta t = 1, 0.5, 0.25$, and 0.125 over time until $T = 900$. The consistent decline observed in all four energy curves signifies a robust numerical solution. This affirms compliance of the system with energy dissipation laws and facilitates the application of larger investigative time steps. In addition, Fig. 1(b) includes two enlarged subgraphs to clearly show the differences between the curves at the turning points. Obviously, the result of $\Delta t = 0.125$ aligns with that for $\Delta t = 0.25$, but differs from results with larger time steps like $\Delta t = 1$ and $\Delta t = 0.5$. Although the difference is less significant for large states, it is recommended to use smaller time steps to obtain more accurate numerical solutions. The additional stability term plays an important role in the gradual stabilization process. We can easily conclude that our numerical solution converges and that the proposed scheme exhibits validity even for large time steps.

4.2. Evolution of the metal powder melt pool on the substrate

In this section, we investigate a simulation of the fabrication process for monolayer printing, focusing specifically on spiral modeling. We place a spotlight on the magnification of this single-layer process, which allows us to deeply explore the phase transition outcomes that arise from the interaction between the powder and the substrate. This exploration unveils the fascinating phenomena associated with the evolution of the melt pool. Our simulation effectively illustrates that when each line in a single-layer printing undergoes fusion, the outcome is quite satisfactory. Furthermore, there is an impressive coupling of temperature distribution. Fig. 2 sequentially showcases the printing effects of the single-layer spiral at specific time points $t = 1, 2, 2.5$, and 3 , respectively.

After that, we shift our focus to the magnification of the single-layer manufacturing process. To conduct a deep investigation into the phase transition outcomes triggered by the powder-substrate interaction, thereby further probing into the phenomena of melt pool evolution. We first consider that the substrate is composed of the same material as the powder. Inspired by [10], we introduce another state variable $0 \leq \psi \leq 1$ to track the degree of solidification of the metal, thereby distinguishing the powder from the fully dense phase. The consolidation parameter, symbolized as ψ , is set to 1 in areas of complete density and 0 in powdered zones. This

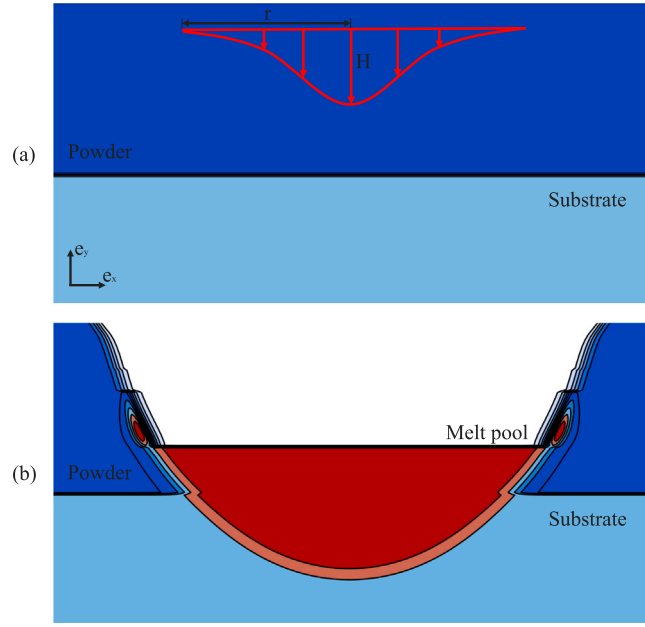


Fig. 3. Schematic representation of the molten pool formed as a result of the phase transition of the powder-matrix interaction in the SLM process. (a) is a two-dimensional schematic diagram of the SLM process. The dark blue area represents the metal powder and the light blue area represents the substrate. The red solid line represents the Gaussian laser beam and the black solid line represents the contour. (b) is a schematic diagram of the melt pool formed in the SLM process. The red area represents the melt pool, the dark blue area represents the metal powder, and the light blue area represents the substrate, the black solid line represents the contour line.

parameter is closely linked with the trajectory and present state of phase parameters at each material point, preserving the peak value of ϕ . When the powder is completely melted ($\phi = 1$), the material at that location is considered to become completely dense. Therefore, $\psi = 1$ at this point and will remain completely dense. For materials that are only partially melted, where $0 < \phi < 1$, the material is not deemed fully consolidated, and ψ reflects the highest value of ϕ . In general, ψ takes the maximum value of the current value ψ or the peak value of ϕ at any time at a given position $x \in \Omega$, as shown below:

$$\psi(x, t) = \max_{0 \leq t' \leq t} \left(\phi(x, t'), \psi(x, t) \right). \quad (40)$$

Specifically, we combine the two state variables to represent the matter state jointly. We use different combinations of ϕ and ψ to describe non-dense solid metal powder ($\phi = 0, \psi = 0$), dense solid substrate ($\phi = 0, \psi = 1$), and dense melt pool ($\phi = 1, \psi = 1$), respectively. As shown in Fig. 3, according to the material state defined above, we divide the entire computational domain into two regions, the dark blue region for the metallic powder and the light blue region for the substrate. A layer of metallic powder is laid on the substrate surface to study its heat transfer and interface dynamics under vertical irradiation by a laser beam at a fixed position. As a heat source, a pulsed Gaussian laser beam is vertically irradiated downward above the metallic powder layer, providing intermittent high temperatures. In view of the heat source caused by the laser in the system, it is necessary to add a heat source term \dot{Q} in the heat conduction equation to ensure its applicability as follows:

$$\frac{\partial e}{\partial t} = -\nabla \cdot \left(M_e \nabla \frac{\delta S}{\delta e} \right) + \dot{Q}. \quad (41)$$

We give a comprehensive explanation of the existing control equations and make corresponding modifications. The heat source term \dot{Q} is composed of radiation loss \dot{Q}_r and laser irradiation \dot{Q}_{ir} , so Eq. (13b) can be rewritten as follows:

$$\frac{\partial T}{\partial t} + M_\phi \frac{L_a}{TT_m} p'(\phi) \frac{\partial \phi}{\partial t} = k \Delta T + \dot{Q}_r + \dot{Q}_{ir}, \quad (42)$$

where

$$\dot{Q}_r = -\frac{\beta \sigma (T^4 - T_m^4)}{\epsilon}, \quad \dot{Q}_{ir} = -\frac{\alpha H \cdot n}{\epsilon}, \quad (43)$$

$$H = -\frac{\sqrt{2/\pi} Q}{r} \exp\left(\frac{-2(x - x_c - U_r t)^2}{r^2}\right) e_y. \quad (44)$$

Here β is the emissivity, σ is the Stefan-Boltzmann constant, α is the powder absorption rate constant, n is the surface normal vector, H is the two-dimensional Gaussian laser irradiation flux, \dot{Q} is the average laser power per unit length, x_c is the laser focus projected on the x -axis, e_y is the unit vector parallel to the y -axis, and U_r is the speed of the nozzle in the horizontal direction. It is worth

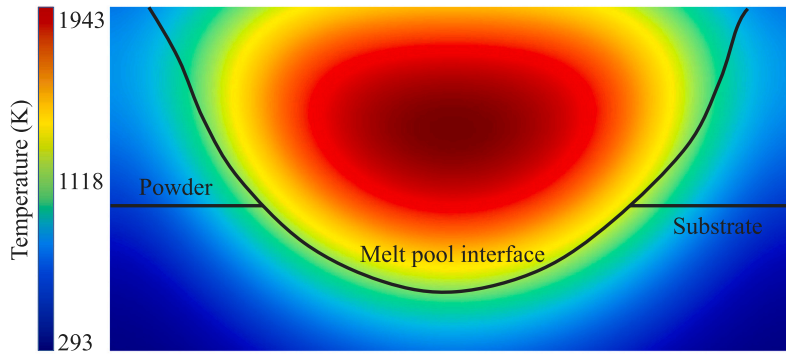


Fig. 4. Temperature distribution diagram of molten pool formed by powder-substrate in SLM process. Solid black lines indicate the interface between molten pool and substrate.

noting that after introducing the laser beam as a heat source, the system we mention earlier is no longer an isolated closed system, which is likely to lead to the collapse of the energy dissipation theorem. In this section, we set the average power of the laser to $\bar{Q} = 1.9 \times 10^5$ W/m and the scanning speed of the nozzle to 0.1 m/s. As shown in Fig. 3(a), a fixed Gaussian laser beam is projected vertically downward onto the metal powder layer, providing heat perpendicular to the substrate. Fig. 3(b) shows the melt pool formed by the phase transition results of the powder-substrate interaction. We can clearly see that under the effect of a vertically projected laser beam heat source, the powder-substrate interface undergoes a deformation due to the combined effect of thermal and surface tension, which leads to the formation of a melt pool. By introducing phase and solidification parameters, we are enabled to track the phase transition and variability in material density. This further allows us to ascertain the morphology of the melt pool and the density distribution within the material. As shown in Fig. 4, we present the temperature distribution during the formation of the melt pool. A fixed Gaussian laser irradiates downward onto the layer of metal powder, providing heat perpendicular to the substrate. The energy is concentrated in a small area and diffuses outward. The temperature distribution aligns with the mechanism in the SLM process where the laser transfers energy to the metal powder and then diffuses outward, which is consistent with the processing scenario. The black solid line in Fig. 4 delineates the interface between the melt pool and the substrate.

4.3. Simulation manufacturing process for layer-by-layer printing modeling

In this section, we simulate the staged evolution effect of the rabbit model manufactured layer by layer under the guidance of the algorithm through simulation experiments, as shown in Fig. 5. In real SLM manufacturing, the digital model of the STL file of the prepared part is mathematically sliced into thin layers, and then the metal powder is deposited layer by layer, with each layer corresponding to a slice of the model. Between two consecutive powder layers, the laser beam scans the layers based on STL file design data and selectively melts the powder. Complex components are constructed layer by combining power layer deposition and laser melting methods. Notably, our algorithm employs a layer-by-layer analysis strategy. It begins by interpreting the G-code data of the 3D model. Subsequently, it generates a point cloud connection matrix. The motion trajectory of the laser beam is then designed. This allows us to simulate the formation of liquid droplets, which result from the layer-by-layer melting of metal powder under specific SLM process parameters. Our method is adaptable to various scanning strategies and process parameters, each yielding distinct print effects. The algorithm effectively captures and displays the nuanced differences between them.

4.4. Influence of scan radius on layer-by-layer fabrication simulation

In this section, we compare the staged evolution simulation effects of the gear model under different scanning radii through simulation experiments. Our model and algorithm are adaptable to varying scanning radii, with different radii yielding distinct print effects for the model. To validate the impact of different scanning radii on the simulated printing effect, we conduct numerical experiments at different scanning radii of 0.2, 0.1, and 0.05. As shown in Fig. 6, we compare the stage-by-stage printing results of the gear model under different scanning radii of 0.2, 0.1 and 0.05. When employing a larger scanning radius, such as 0.2, it becomes evident that the extended scanning radius facilitates effective heat dissipation. This results in a larger temperature gradient, significantly impacting the non-physical deformation in the scanning vector direction. However, the simulation time required is shorter, and the efficiency is higher. When a shorter scanning radius such as 0.05 is used, a uniform temperature field is often generated, resulting in a finely compact model, but the simulation time is longer, and the efficiency is lower.

4.5. Evolutionary experiments simulating the layer-by-layer printing with different supports

In this section, we compare the simulation outcomes of the glasses model at various evolutionary stages, considering unsupported, tree, and normal supported scenarios. Fig. 7(a) to (c) show the stage-by-stage display of the glasses model under flat without

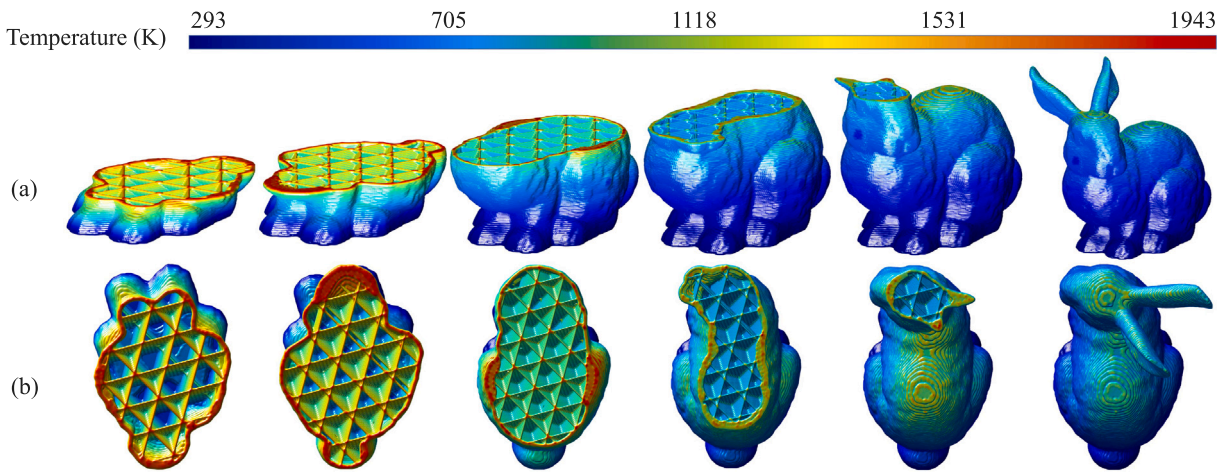


Fig. 5. The stage evolution simulation effect of layer-by-layer printing of the rabbit model. (a) in front view and (b) in top view.

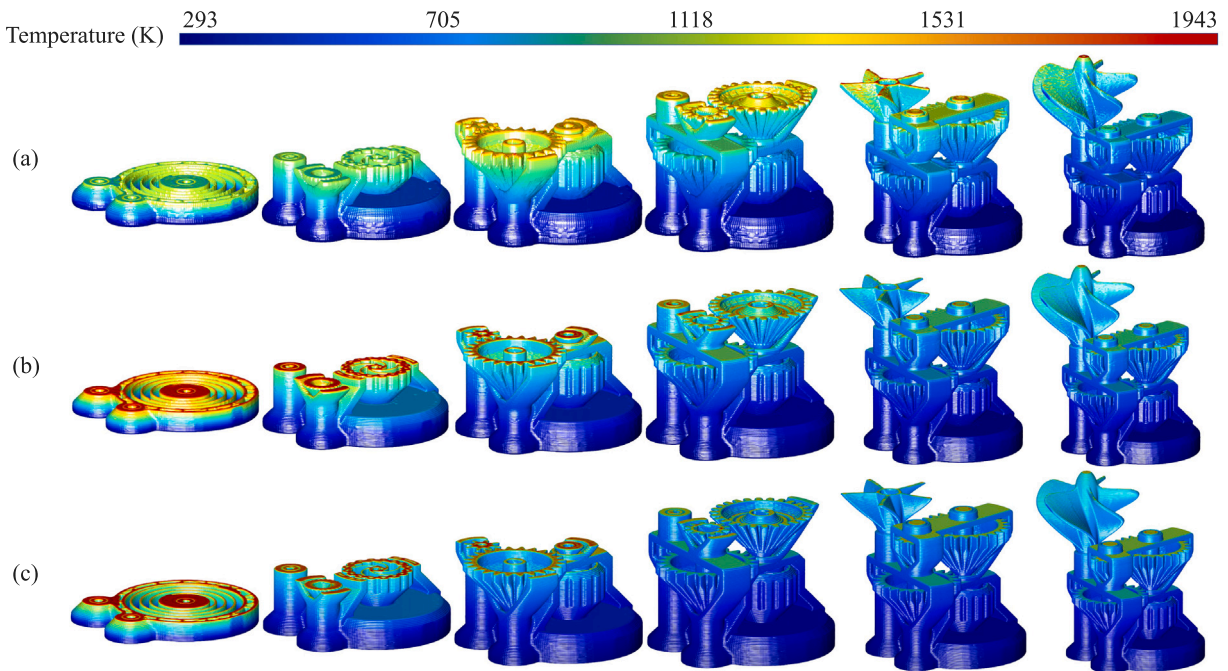


Fig. 6. The stage effect of layer-by-layer printing of the gear model under different scanning radii. (a) to (c) are the stage effects of simulating the layer-by-layer printing of the gear model when the scanning radius is 0.2, 0.1, and 0.05, respectively.

support, with tree-shaped support, and with normal support, respectively. In Fig. 7(a), the horizontally placed glasses model can be formed by relying on its own supporting force without adding a support structure. In the realm of SLM fabrication, the strategic placement of parts is paramount for achieving structural finesse and superior quality. Regions requiring high surface quality require meticulous machining to maintain quality and limit overhangs. With optimal placement, we can reduce the volume of machined material, limit superfluous supports, and guarantee the quality of the parts. Fig. 7(b) and (c) depict the sequential simulation of a glasses model, tilted at 45 degrees, supported by tree-shaped and standard structures, respectively. The inherent layer-by-layer principle of SLM gives rise to overhangs that mandate support. These supports are instrumental in not only enabling the formation of overhang features, but also in shouldering the weight of the parts, mitigating horizontal deformation, and promoting heat dissipation. Furthermore, they modulate the local temperature during the printing process by introducing additional heat conduction pathways. The glasses model with support Fig. 7(b) and (c) can dissipate heat more effectively during the local forming process, and the cooling rate is higher than that of the glasses model without support Fig. 7(a). Our algorithm is able to model the temperature

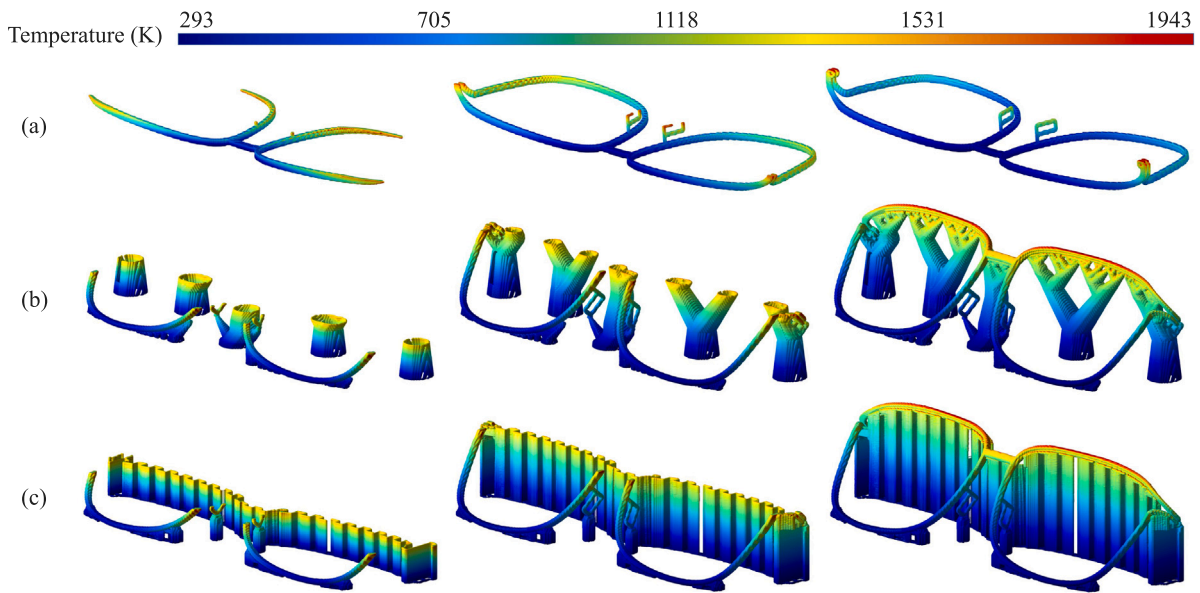


Fig. 7. Simulation of the printing effect of the glasses model in different placement positions and with added support. (a) to (c) are the stage effects of evolution and temperature distribution of the glasses model in the flat without support, with tree-like support, and with normal support, respectively. In (a), the horizontally placed glasses model can be formed by relying on its own support force without adding a support structure. In (b) and (c), the stage simulation of the printing evolution of the glasses model placed at a 45-degree tilt with tree-like support and normal support is shown.

profile and layer-by-layer formation effects in SLM fabrication wells for different models with different placement and different types of supports.

4.6. Comparative simulations of layer-by-layer printing with different powder layer thickness

In this section, we compare the simulation effects of the vase model at different stages of evolution through simulations with different powder layer thicknesses. Our model and algorithm can be adapted to different powder layer thicknesses, but different powder layer thicknesses lead to different print effects of the model. To verify the effect of different powder layer thicknesses on the printing effect of the digital model, we perform simulations with three different powder layer thicknesses of 0.4, 0.2, and 0.1. As shown in Fig. 8, we compare the schematic results for the outer face and profile of the layer-by-layer printed vase model at three different powder layer thicknesses of 0.4, 0.2, and 0.1. Fig. 8(a) to (c) are schematic diagrams of the printing effect of the vase digital model when the powder layer thickness is 0.4, 0.2, and 0.1, respectively. In Fig. 8(a), the vase digital model is sliced into 40 layers with a powder layer thickness of 0.4. In Fig. 8(b), the vase digital model is sliced into 79 layers with a powder layer thickness of 0.2. In Fig. 8(c), the vase digital model is sliced into 158 layers with a powder layer thickness of 0.1.

The SLM manufacturing process directly melts metal powder layer by layer (the thickness of each layer of powder is the same as the slicing thickness). On each layer, the scanning laser beam provides energy to locally melt a layer of deposited metal powder and fuse it onto the previously melted layer. Clearly, when slicing a vase model of the same size, a greater slicing thickness results in fewer required layers, while a smaller slicing thickness leads to more layers. The associated data storage space also varies, being larger for smaller slicing thicknesses. In addition, we can see that under the condition of a larger layer thickness, after the powder layer is melted, larger droplets are obtained, the internal structure is slightly unstable, defects and air entrapment are more likely to occur, and there is a lack of fusion between the two required laser scans, and individual layers may be suspended. Under the condition of a smaller layer thickness, the powder layer is melted and filled into the gaps between the powders to obtain smaller droplets. The internal structure, enriched with particles, forms a stable configuration that minimizes the likelihood of voids or air entrapment. Therefore, choosing a suitable powder layer thickness is crucial to the manufacturing effect. Our algorithm provides an efficient way to choose the appropriate layer thickness. Further research helps optimize the printing parameters of the digital model to achieve higher quality SLM manufacturing results.

5. Conclusion

In this study, we developed a numerical model based on phase-field theory, which accurately simulates key physical phenomena such as solid-liquid phase changes and heat conduction during the SLM process. The establishment of the model was based on the variational principle of minimizing the free energy functional, which formed a complete coupled system that could simultaneously capture multiple physical quantities such as temperature fields and interface morphology. We discretized the model using the

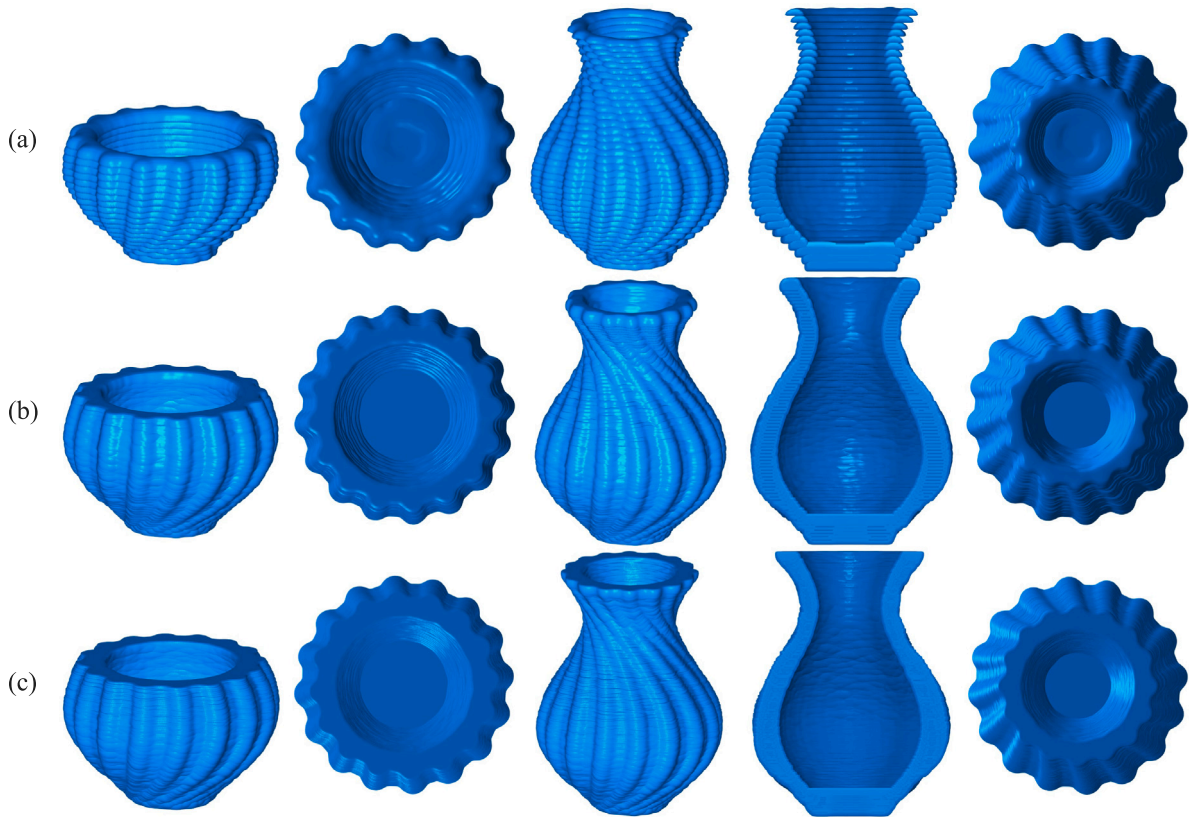


Fig. 8. Simulation of the external measurement and cross-sectional effects of layer-by-layer printing of the vase model under different layer thicknesses. (a) to (c) are schematic diagrams of the printing effects when the layer thickness is 0.4, 0.2, and 0.1, respectively. The first and second columns are the outer schematic diagram and the top view of the cross section when half of the layers are printed, and the third to fifth columns are the outer schematic diagram, the front view of the vertical cross section, and the top view of the outer surface after all layers are printed.

semi-implicit Crank–Nicolson scheme. This ensured second-order accuracy and unconditional energy stability, which are crucial for maintaining numerical stability and the physical rationality of the solution. Through numerical experiments, we demonstrated the high-precision capture ability of the model for interface morphology and temperature fields, verifying the effectiveness and superiority of the model. Furthermore, we developed a digital model that mirrors the actual manufacturing process. This model is capable of effectively simulating the temperature distribution and morphological changes of the components fabricated during the SLM process. It thereby provides a dependable basis for forecasting and enhancing the quality and performance of parts produced through SLM additive manufacturing. The complexity of coupled systems, particularly when modeling large or long-duration processes with complex geometries or substantial components, significantly increases the need for computational resources. This need motivates us to seek more computationally efficient approaches to reduce resource usage and make extensive simulations more feasible. In addition, the accuracy of the model depends on accurate physical parameter inputs, which can be difficult and uncertain to obtain. To address this challenge, we must refine our parameter estimation and calibration techniques. By utilizing experimental data and strengthening the bond between data and model, we can decrease our dependence on exact parameter inputs. This is also an issue that we aim to address in our future work.

CRediT authorship contribution statement

Sijing Lai: Writing – original draft, Visualization, Software, Methodology, Investigation, Formal analysis, Data curation, Conceptualization. **Qing Xia:** Writing – original draft, Methodology, Formal analysis, Conceptualization. **Junseok Kim:** Writing – review & editing, Supervision, Investigation, Conceptualization. **Yibao Li:** Writing – review & editing, Supervision, Methodology, Funding acquisition, Conceptualization.

Declaration of competing interest

The authors declare that they have no known competing financial interests or personal relationships that could have appeared to influence the work reported in this paper.

Data availability

No data was used for the research described in the article.

Acknowledgments

This work is supported by National Natural Science Foundation of China (No. 12271430). The authors would like to thank the reviewers for their constructive and helpful comments regarding the revision of this article.

References

- [1] Abdulhameed O, Al-Ahmari A, Ameen W, Mian S. Additive manufacturing: Challenges, trends, and applications. *Adv Mech Eng* 2019;11:1687814018822880.
- [2] Liu J, Dong S, Jin X, Wu P, Yan S, Liu X, Tan Y, Li C, Xu B. Quality control of large-sized alloy steel parts fabricated by multi-laser selective laser melting (ML-SLM). *Mater Des* 2022;223:111209.
- [3] Alinejadian N, Kazemi S, Odnevall Inger. SLM-processed MoS₂/MoS₂S₃ nanocomposite for energy conversion/storage applications. *Sci Rep* 2022;12:5030.
- [4] Parhizi M, Zhou L, Jain A. Theoretical modeling of solid-liquid phase change in a phase change material protected by a multilayer Cartesian wall. *Int J Heat Mass Transfer* 2022;197:123330.
- [5] Gu H, Wei C, Li L, Han Q, Setchi R, Ryan M, Li Q. Multi-physics modelling of molten pool development and track formation in multi-track, multi-layer and multi-material selective laser melting. *Int J Heat Mass Transfer* 2020;151:119458.
- [6] Wang Z, Yan W, Liu W, Liu M. Powder-scale multi-physics modeling of multi-layer multi-track selective laser melting with sharp interface capturing method. *Comput Mech* 2019;63:649–61.
- [7] Ali H, Ghadbeigi H, Mumtaz K. Processing parameter effects on residual stress and mechanical properties of selective laser melted Ti6Al4V. *J Mater Eng Perform* 2018;27:4059–68.
- [8] Xiao Z, Chen C, Zhu H, Hu Z, Nagarajan B, Guo L, Zeng X. Study of residual stress in selective laser melting of Ti6Al4V. *Mater Des* 2020;193:108846.
- [9] Wang SL, Sekerka RF, Wheeler AA, Murray BT, Coriell SR, Braun RJ, McFadden GB. Thermodynamically-consistent phase-field models for solidification. *Phys D* 1993;69:189–200.
- [10] Roy S, Juha M, Shephard MS, Maniatty AM. Heat transfer model and finite element formulation for simulation of selective laser melting. *Comput Mech* 2018;62:273–84.
- [11] Li Y, Wang K, Yu Q, Xia Q, Kim J. Unconditionally energy stable schemes for fluid-based topology optimization. *Commun Nonlinear Sci Numer Simul* 2022;111:106433.
- [12] Bouabbou A, Vaudreuil S. Understanding laser-metal interaction in selective laser melting additive manufacturing through numerical modelling and simulation: a review. *Virt Phys Prototy* 2022;17:543–62.
- [13] Heeling T, Cloots M, Wegener K. Melt pool simulation for the evaluation of process parameters in selective laser melting. *Addit Manuf* 2017;14:116–25.
- [14] Long T, Huang H. An improved high order smoothed particle hydrodynamics method for numerical simulations of selective laser melting process. *Eng Anal Bound Elem* 2023;147:320–35.
- [15] Krzyzanowski M, Svyetlichnyy D. A multiphysics simulation approach to selective laser melting modelling based on cellular automata and lattice Boltzmann methods. *Comput Part Mech* 2022;9:117–33.
- [16] Ma J, Niu X, Zhou Y, Li W, Liu Y, Shen M, Wang H, Cheng W, You Z. Simulation of solidification microstructure evolution of 316L stainless steel fabricated by selective laser melting using a coupled model of smooth particle hydrodynamics and cellular automata. *J Mater Res Technol* 2023;27:600–16.
- [17] Chen Q, Guillemot G, Gandin CA, Bellet M. Numerical modelling of the impact of energy distribution and Marangoni surface tension on track shape in selective laser melting of ceramic material. *Addit Manuf* 2018;21:713–23.
- [18] Liu D, Wang Y. Mesoscale multi-physics simulation of solidification in selective laser melting process using a phase field and thermal lattice boltzmann model. In: *Int. des. eng. tech. conf. comput. inf. eng. conf.* Vol. 58110, 2017, V001T02A027.
- [19] Carraturo M, Kollmannsberger S, Reali A, Auricchio F, Rank E. An immersed boundary approach for residual stress evaluation in selective laser melting processes. *Addit Manuf* 2021;46:102077.
- [20] Xia Q, Sun G, Yu Q, Kim J, Li Y. Thermal-fluid topology optimization with unconditional energy stability and second-order accuracy via phase-field model. *Commun Nonlinear Sci Numer Simul* 2023;116:106782.
- [21] Wang X, Chou K. Microstructure simulations of inconel 718 during selective laser melting using a phase field model. *Int J Adv Manuf Technol* 2019;100:2147–62.
- [22] Ali B, Heider Y, Markert B. Predicting residual stresses in SLM additive manufacturing using a phase-field thermomechanical modeling framework. *Comput Mater Sci* 2024;231:112576.
- [23] Xia Q, Kim J, Li Y. Modeling and simulation of multi-component immiscible flows based on a modified Cahn-Hilliard equation. *Eur J Mech B Fluids* 2022;95:194–204.
- [24] Xie W, Li Y. A novel estimation method for microstructural evolution based on data assimilation and phase field crystal model. *Commun Nonlinear Sci Numer Simul* 2023;127:107562.
- [25] Chen L. Phase-field models for microstructure evolution. *Annu Rev Mater Res* 2002;32:113–40.
- [26] Li Y, Yu Q, Ham S, Kwak S, Lee C, Kim J. A phase-field model without artificial curvature effect for the crystal growth simulation. *Int J Heat Mass Transfer* 2023;203:123847.
- [27] Steinbach I. Phase-field model for microstructure evolution at the mesoscopic scale. *Annu Rev Mater Res* 2013;43:89–107.
- [28] Li Y, Kim J. Phase-field simulations of crystal growth with adaptive mesh refinement. *Int J Heat Mass Transfer* 2012;55(25–26):7926–32.
- [29] Sessim M, Shi L, Philippot SR, Tonks MR. Phase-field modeling of carbon fiber oxidation coupled with heat conduction. *Comput Mater Sci* 2022;204:111156.
- [30] Zhang L, Tonks MR, Millett PC, Zhang Y, Chockalingam K, Biner B. Phase-field modeling of temperature gradient driven pore migration coupling with thermal conduction. *Comput Mater Sci* 2012;56:161–5.
- [31] August A, Ettrich J, Rölle M, Schmid S, Berghoff M, Selzer M, Nestler B. Prediction of heat conduction in open-cell foams via the diffuse interface representation of the phase-field method. *Int J Heat Mass Transfer* 2015;84:800–8.
- [32] Sahoo S, k Chou. Phase-field simulation of microstructure evolution of Ti-6Al-4V in electron beam additive manufacturing process. *Addit Manuf* 2016;9:14–24.
- [33] Liu S, Shin YC. Integrated 2D cellular automata-phase field modeling of solidification and microstructure evolution during additive manufacturing of Ti6Al4V. *Comput Mater Sci* 2020;183:109889.
- [34] Yang Y, Kühn P, Yi M, Egger H, Xu BX. Non-isothermal phase-field modeling of heat-melt-microstructure-coupled processes during powder bed fusion. *JOM* 2020;72:1719–33.

- [35] Yang Y, Ragnvaldsen O, Bai Y, Yi M, Xu B. 3D non-isothermal phase-field simulation of microstructure evolution during selective laser sintering. *NPJ Comput Mater* 2019;5:81.
- [36] Xia Q, Sun G, Kim J, Li Y. Multi-scale modeling and simulation of additive manufacturing based on fused deposition technique. *Phys Fluids* 2023;35.
- [37] Steinbach I. Phase-field models in materials science. *Model Simul Mater Sci* 2009;17:073001.
- [38] Xia B, Mei C, Yu Q, Li Y. A second order unconditionally stable scheme for the modified phase field crystal model with elastic interaction and stochastic noise effect. *Comput Methods Appl Mech Engrg* 2020;363:112795.
- [39] Jiang B, Xia Q, Kim J, Li Y. Efficient second-order accurate scheme for fluid–surfactant systems on curved surfaces with unconditional energy stability. *Commun Nonlinear Sci Numer Simul* 2024;135:108054.
- [40] Xiao X, Feng X. A second-order maximum bound principle preserving operator splitting method for the Allen–Cahn equation with applications in multi-phase systems. *Math Comput Simulation* 2022;202:36–58.
- [41] Cheng Q, Liu C, Shen J. A new interface capturing method for Allen–Cahn type equations based on a flow dynamic approach in Lagrangian coordinates, I. One-dimensional case. *J Comput Phys* 2020;419:109509.
- [42] Li X, Shen J. Stability and error estimates of the SAV Fourier-spectral method for the phase field crystal equation. *Adv Comput Math* 2020;46:1–20.
- [43] Xia Q, Kim J, Xia B, Li Y. An unconditionally energy stable method for binary incompressible heat conductive fluids based on the phase-field model. *Comput Math Appl* 2022;123:26–39.
- [44] Li Y, Kim J. An efficient and stable compact fourth-order finite difference scheme for the phase field crystal equation. *Comput Mech* 2017;319:194–216.
- [45] Cheng J, Xia Q, Kim J, Li Y. An efficient linear and unconditionally stable numerical scheme for the phase field sintering model. *Commun Nonlinear Sci Numer Simul* 2023;127:107529.
- [46] Xia Q, Liu Y, Kim J, Li Y. Binary thermal fluids computation over arbitrary surfaces with second-order accuracy and unconditional energy stability based on phase-field model. *J Comput Appl Math* 2023;433:115319.
- [47] Li Y, Kim J, Wang N. An unconditionally energy-stable second-order time-accurate scheme for the Cahn–Hilliard equation on surfaces. *Commun Nonlinear Sci Numer Simul* 2017;53:213–27.
- [48] Li Y, Yang J. Consistency-enhanced SAV BDF2 time-marching method with relaxation for the incompressible Cahn–Hilliard–Navier–Stokes binary fluid model. *Commun Nonlinear Sci Numer Simul* 2023;118:107055.
- [49] Han D, Bylev A, Yang X, Tan Z. Numerical analysis of second order, fully discrete energy stable schemes for phase field models of two-phase incompressible flows. *J Sci Comput* 2017;70:965–89.
- [50] Yang J, Chen J, Tan Z. Highly efficient variant of SAV approach for two-phase incompressible conservative Allen–Cahn fluids. *Eng Comput* 2022;38(6):5339–57.
- [51] Conti M. Solidification of binary alloys: Thermal effects studied with the phase-field model. *Phys Rev E* 1997;55:765.
- [52] Xia Q, Yang J, Kim J, Li Y. On the phase field based model for the crystalline transition and nucleation within the Lagrange multiplier framework. *J Comput Phys* 2024;113158.
- [53] Li Y, Qin K, Xia Q, Kim J. A second-order unconditionally stable method for the anisotropic dendritic crystal growth model with an orientation-field. *Appl Numer Math* 2023;184:512–26.
- [54] Horn RA, Zhang F. Basic properties of the Schur complement. *Schur comp. appl.*, Boston, MA: Springer US; 2005, p. 17–46.
- [55] Gallier J. The Schur complement and symmetric positive semidefinite (and definite) matrices. *Penn Eng* 2010;1–12.